ICANS-XV
15th Meeting of the International Collaboration on Advanced Neutron Sources
November 6-9, 2000
Tsukuba, Japan

5.3
Progress in Design of the SNS Linac

R. Hardekopf [1*] for the SNS linac design team[1]

[1] Los Alamos National Laboratory, Los Alamos, NM, 87545, USA
* E-mail: hardekopf@lanl.gov

Abstract

The Spallation Neutron Source (SNS) is a six-laboratory collaboration to build an intense pulsed neutron facility at Oak Ridge, TN. The linac design has evolved from the conceptual design presented in 1997 in order to achieve higher initial performance and to incorporate desirable upgrade features. The linac is now designed to produce 2-MW beam power using a combination of radio-frequency quadrupole (RFQ) linac, drift-tube linac (DTL), coupled-cavity linac (CCL), and superconducting–RF (SRF) linac. Designs of each of these elements support the high peak intensity and high quality beam required for injection into the SNS accumulator ring. This paper will trace the evolution of the linac design and the progress made in the R&D program.

1. Introduction

The SNS project had its conceptual design review in June 1997 and received construction funding from the US Department of Energy in October 1998. The original design of the 1-GeV linear accelerator (linac) was a room-temperature device that could deliver average beam currents from 1 to 4 mA to the accumulator ring that follows. This baseline design would have provided 1 MW of beam power, but the accelerator system was upgradeable to 2 and 4 MW. This design and the upgrade requirements were described in several early papers [1-4]. The basic requirements and design features are shown in Tables 1 and 2.

Table 1. Linac requirements at CDR

Input H^- energy	2.5 MeV
Output H^- Energy	1001 MeV
Average beam current	1.04 mA
Average beam power	1.04 MW
Macropulse repetition rate	60 Hz
Macropulse length	0.974 ms
Beam duty factor	5.84 %
Chopper transmission	65%
Chopper period	841 ns
Peak macropulse current	27.7 mA
Avg. macropulse current	18.0 mA
Beam losses	<1 nA/m at 1 GeV

Table 2. Original linac design parameters

RF duty factor	7.02%
Average accelerating gradient E_0T	2.7 MV/m
Avg. Energy gain / real estate meter	2.02 MeV/m
Peak structure power losses	80.7 MW
Peak installed RF power	142.5 MW
Average RF power to linac	6.74 MW
Specified ac wall power for RF	22 MW
No. of 1.25-MW 402.5-MHz klystrons	2
No. of 2.5-MW 805-MHz klystrons	56
Physical length of linac	495 m
Linac vacuum	$<1 \times 10^{-7}$ torr
Linac tunnel, width × height	14 × 10 ft

The evolution of the room-temperature-linac design from 1997 to 1999 is described in [5] with engineering overviews in [6-8]. The 2-MW upgrade could be achieved with only the addition of RF power, but 4 MW required a second ion source and 402.5-MHz front-end system up to 20 MeV, with funneling of the two beams into an 805-MHz coupled-cavity drift-tube linac (CCDTL) structure.

Following an intensive project review late in 1999, the baseline design was changed to a 2-MW linac without provision for upgrading to 4-MW. This allowed the elimination of one of the RF structures, the CCDTL, by extending the 402.5-MHz DTL up to about 87 MeV. At this energy, the beam could be injected directly into the CCL structure. This change was formally adopted in November 1999. The following March, after several studies of superconducting technology applied to the SNS linac, the baseline was changed to a superconducting RF (SRF) linac beginning at 186 MeV [9,10]. Subsequent optimization of this design has led to the configuration in Figure 1 with overall parameters in Table 3.

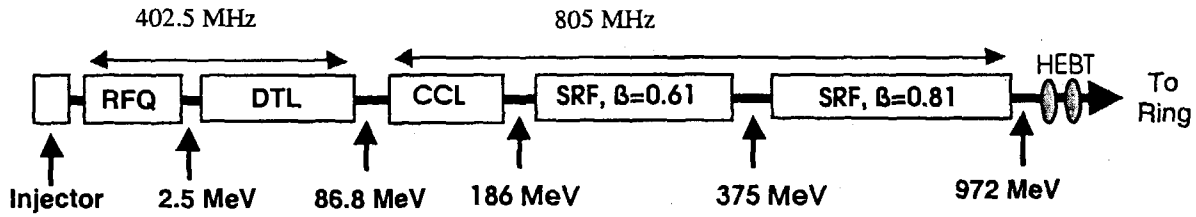

Figure 1. Layout of the present SNS linac. The RFQ, DTL, and CCL are warm structures, and the two SRF regions are superconducting. The energies are at the end of each structure.

Table 3. Parameters of key components for SRF linac baseline, Oct. 2000

Component	Units	2-MW value
H^- ion source	Peak current	65 mA
2.5-MeV RFQ	Peak current	52 mA
Fast choppers – 2 (chopper & anti-chopper)	Beam-on duty factor	68%
87-MeV, 402.5-MHz DTL	tanks	6
186-MeV, 805-MHz CCL	RF modules	4
375-MeV, β=0.61 SRF cavities in 11 cryostats	RF modules	33
1000-Mev, β =0.81 SRF cavities in 15 cryostats	RF modules	59
402,5-MHz, 2.5-MW klystrons (incl. RFQ)	number	7
805-MHz, 5.0-MW klystrons (incl. HEBT)	number	6
805-MHzz, 550-kW klystrons	number	92
Total installed RF peak power	MW	93

Many of the other linac parameters (e.g., repetition rate and duty factor) remained the same, but with the SRF linac we are now able to attain 2-MW with much less RF power. Because of project cost constraints, the energy of the linac will initially be somewhat less than 1 GeV (with fewer high beta SRF cavities installed), and the initial design power will be about 1 MW. However, space is provided in the linac tunnel to increase the energy by adding additional SRF sections when funding permits. Depending on SRF cavity performance and addition of cavities and RF power, an energy of 1.3 GeV or higher may eventually be achieved. The following sections describe the design status of the room-temperature linac. The SRF linac design is described in accompanying papers at this conference [11,12].

2. Front-End System and Chopper

The front-end system, including the H- ion source (65 keV), RFQ linac (2.5 MeV), and medium-energy beam transport (MEBT) is being designed and built by Lawrence Berkeley Laboratory, one of the partners in the SNS collaboration. This injector, most recently described in [13], will deliver a chopped, high-brightness H^- beam to the DTL with peak intensities of 52 mA. The beam transport from the RFQ to the DTL is described in [14].

A key requirement of the linac and accumulator ring design is the ability to cleanly chop the beam to provide a gap in the stored beam in the ring for extraction. Because SNS will operate at higher peak intensities than any existing spallation source, forming this gap and keeping it clear of particles at a level less than 10^{-4} of the peak beam is critical for reducing radiation levels in the ring and subsequent activation of ring components. We are designing a traveling-wave chopper based on the experience at LANSCE, but operating at higher voltage because of the 2.5-MeV beam from the RFQ. Table 4 lists the specifications.

Table 4. MEBT chopper requirements

Beam Energy	2.5 MeV
Chopper length	35 cm
Chopper gap	1.8 cm
Voltage	± 2.35 kV
Deflection angle	18 mrad
Chopping period	945 ns
Rise & fall time	< 10 ns

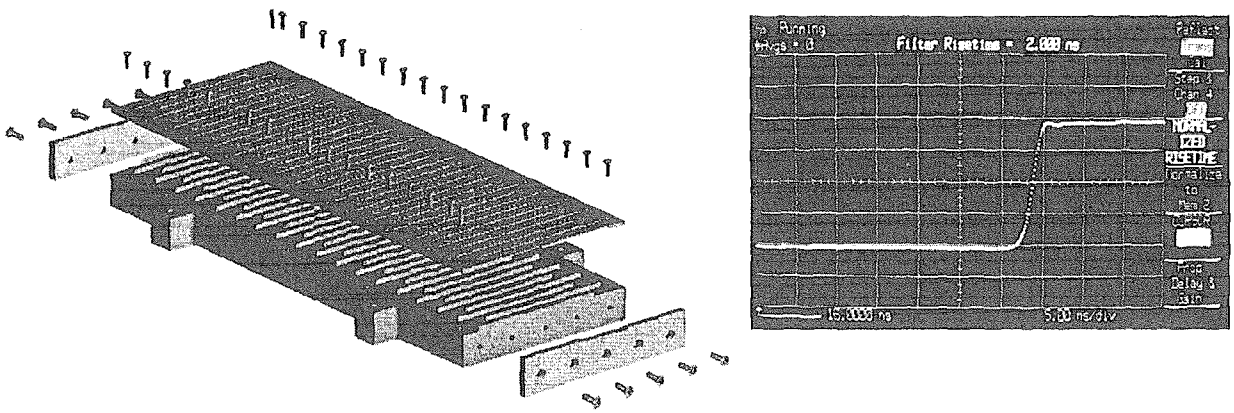

Figure 2. General construction of MEBT chopper on the left with scope trace on the right showing ~2 ns risetime demonstrated on a proof-of-principle structure.

Figures 2 shows general features of the meander-line structure [15-17] currently being developed under the linac R&D program. Performance of a prototype has matched the 3D MAFIA calculations, demonstrating a 50-ohm structure with a risetime of 2 ns. The actual risetime will be limited by the FET pulsers, currently under development at DEI, Inc. in Boulder, CO. The specification for two pulsers to drive the top and bottom meander lines is ± 2500 V with 10-ns (5 to 95%) risetime. Since with this risetime, partially deflected micropulses of the 402.5-MHz beam will be transmitted, an anti-chopper is provided in the

MEBT to return these micropulses to the beam axis before entering the DTL. Figure 3 shows details of the meander-line in the proof-of-principle structure.

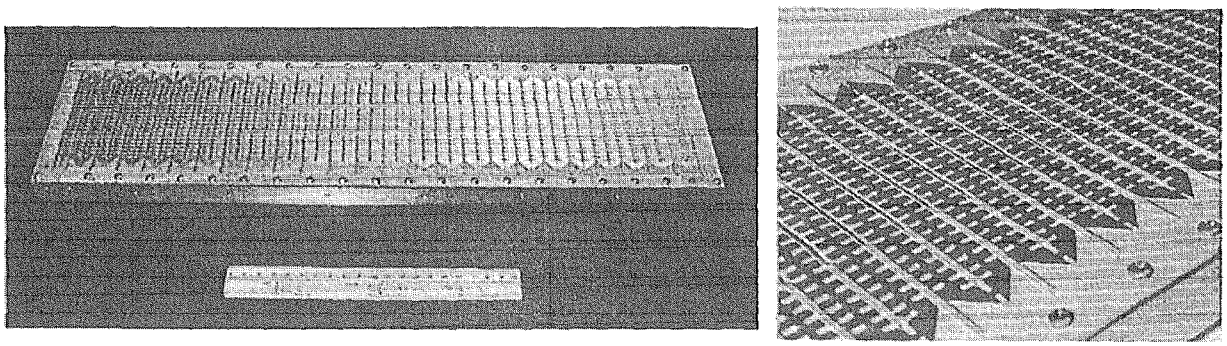

Figure 3. Meander-line structure for the fast MEBT chopper. The proof-of-principle structure is on the left, and a closer view of the etched copper striplines is on the right.

3. Drift-Tube Linac (DTL)

The DTL is divided into 6 tanks, or RF modules. The parameters are summarized in Table 5, and Figure 4 is a cutaway view of the first DTL tank.

Table 5. DTL Design parameters

Structure frequency (MHz)	402.5
Energy (MeV)	86.8
Physical length (m)	36.6
Bore radius (cm)	1.25
Focusing lattice	FFODDO
Lattice period length	$4\beta\lambda$
Accelerating gradient E_0 (MV/m)	3.0
Synchronous phase (deg)	-30
Ave. acceleration rate (MeV/m)	2.3

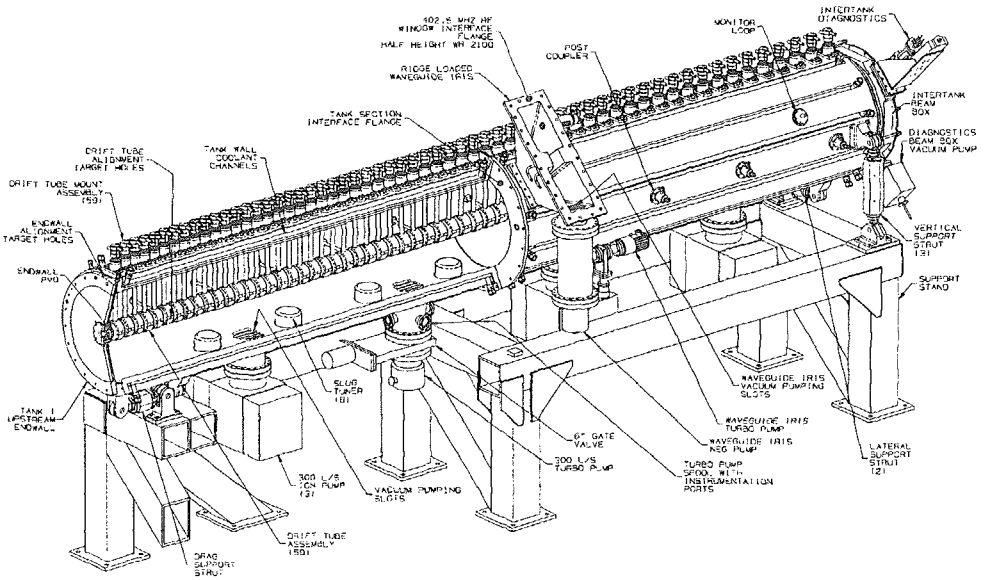

Figure 4. Cutaway view of DTL tank 1.

Each tank is composed of two or three sections along the length that are fastened together using metal seals at the interfaces. The structures consist of copper-plated steel tanks with copper drift tubes mounted on stainless-steel stems. One 2.5-MW klystron powers each tank; and each tank has a separate water-temperature-based resonance-control loop. Permanent-magnet quadrupoles (PMQs) are arranged in a FF0DD0 lattice, which allows placement of electromagnet steering and beam-position diagnostics within the "0" drift tubes. Each tank has a minimum of 4 steering magnets. Post couplers are used at every third drift tube to stabilize the field and to generate a ramp in the first tank for longitudinal matching of the beam from the RFQ and MEBT. Figure 5 shows views of a low-power cold model currently being tested for RF properties

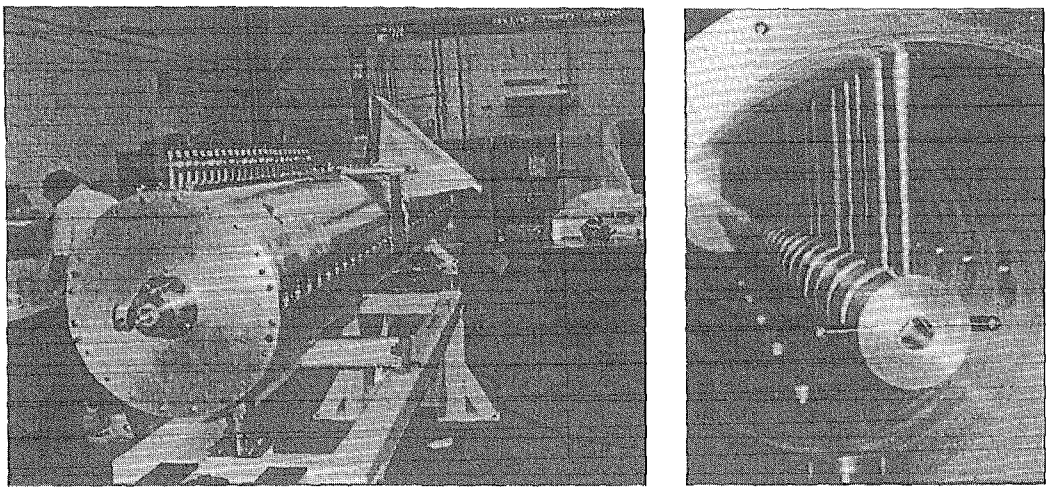

Figure 5. Cold-model assembly for SNS DTL Tank 1.

A preliminary design review of the DTL was held in September 2000. Final design and fabrication are underway, with delivery of the first module scheduled for 2002.

4. Coupled-Cavity Linac (CCL)

The CCL accepts beam from the DTL at 87 MeV and delivers it to the SRF linac at about 186 MeV. The basic parameters are shown in Table 6.

Table 6. CCL Design parameters

Structure frequency (MHz)	805
Final energy (MeV)	185.6
Number of RF modules	4
Number of segments per module	12
Number of cells per segment	8
Physical length (m)	55.4
Bore radius(cm)	1.75
Focusing lattice	F0D0
Lattice period length	$13\beta\lambda$
Accelerating gradient E_0 (MV/m)	3.1 to 3.8
Synchronous phase (deg)	-30 to -26
Ave. acceleration rate (MeV/m)	1.8

Bridge couplers between segments are 3-cell structures of length 2.5 $\beta\lambda$ with

RF feeds through the center cell of the bridge coupler at the 1/4 and 3/4 points of each module. The total thermal load is ~ 1.1 MW at an operational temperature - 80 F. Quadrupole focusing magnets and beam diagnostics are located in the spaces between the segments, and they are supported off the main girder separately from the cavities. Modules will be assembled in a staging area, tuned, and subjected to a series of acceptance tests. When completed, the modules are parted at the central bridge coupler, moved into the tunnel in halves using an engineered transporter, and then reassembled. A series of final tests are conducted in the tunnel as well as connections to the water, RF waveguide and cabling. Figure 6 is an assembly drawing of one of the modules, and figure 7 shows more detail of two segments and the coupling cavity.

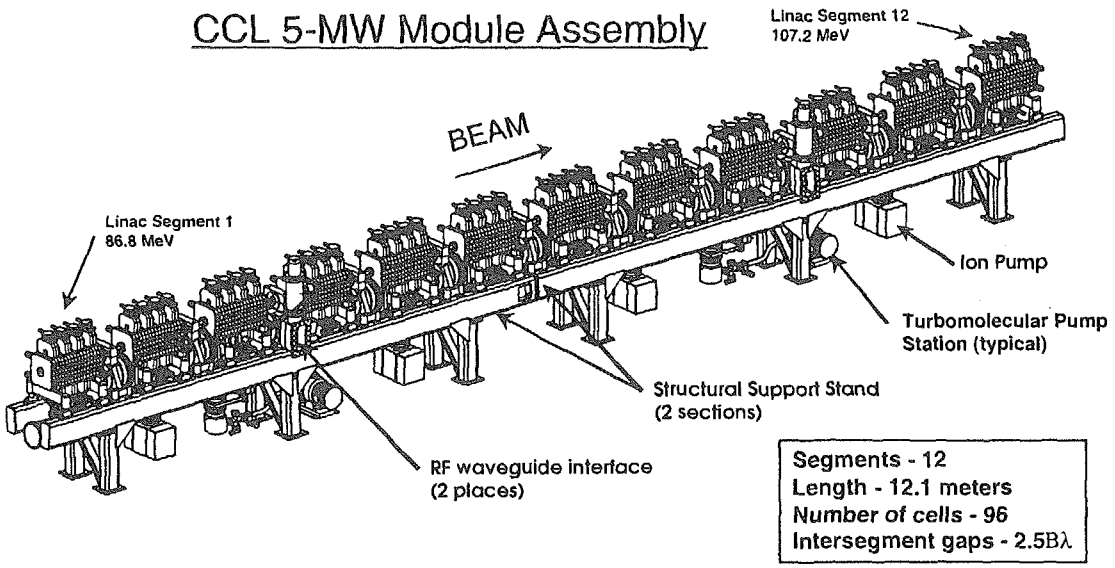

Figure 6. Assembly drawing of the first of four 5-MW CCL modules.

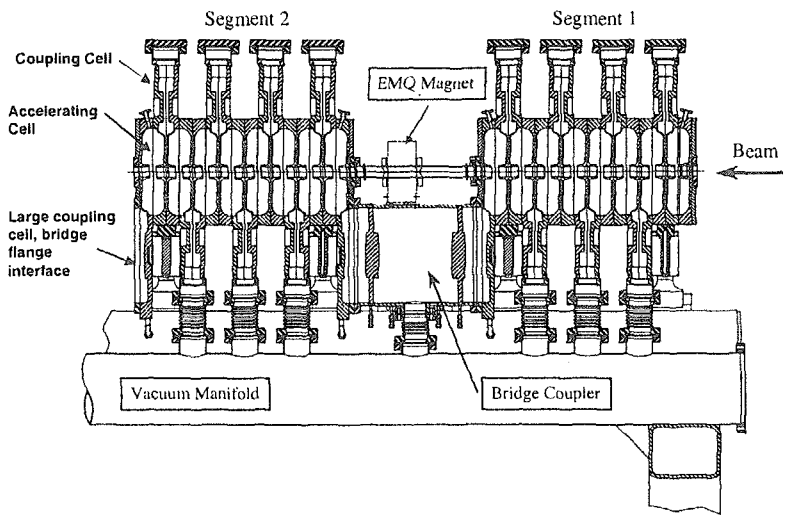

Figure 7. Two 8-cell CCL segments with a bridge coupler.

An R&D program is underway to build both low-power cold models and a powered hot model of the CCL structures. With the cold models, we have tested the RF performance of

accelerating cells, coupling cells and coupling-slot geometry. We are currently testing the bridge-coupler geometry. Figure 8 shows one of the assembled cold models on the bead-pull test stand.

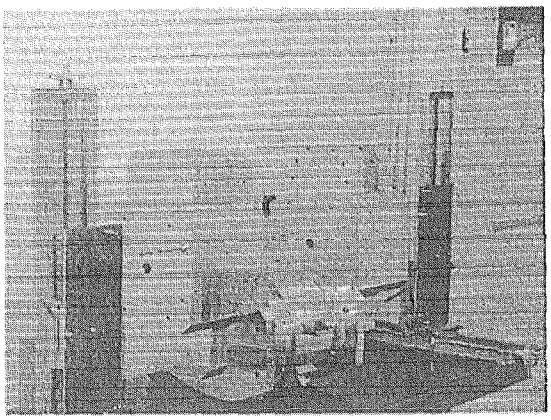

Figure 8. CCL cold-model assembly on the bead-pull test stand.

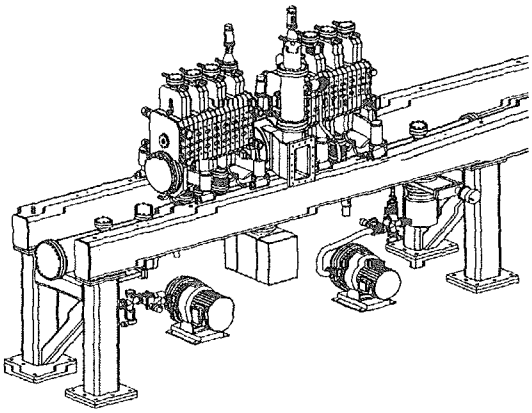

Figure 9. Assembly of the CCL hot Model.

The hot model, shown in Figure 9, consists of two powered segments and a bridge coupler. It will provide verification of the manufacturing and tuning steps as well as thermal stability and vacuum performance. A frequency resonance-control water cart and a prototypical vacuum system are being integrated with the hot model for testing before committing to large-scale fabrication. Parts of the hot model are being fabricated, as shown in the following figures (where a braze alloy is being tested).

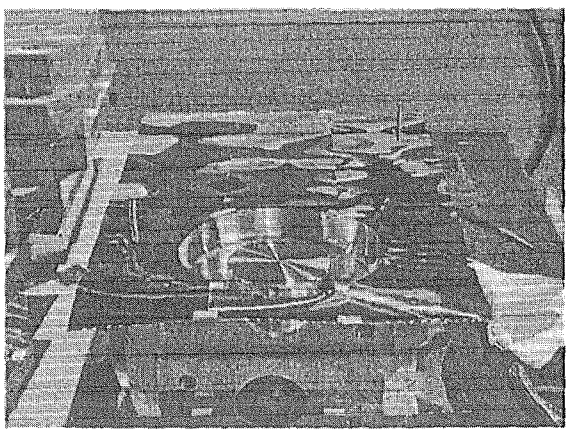

Figure 10. Septum foil lay-up with 50-50, 2-mil alloy.

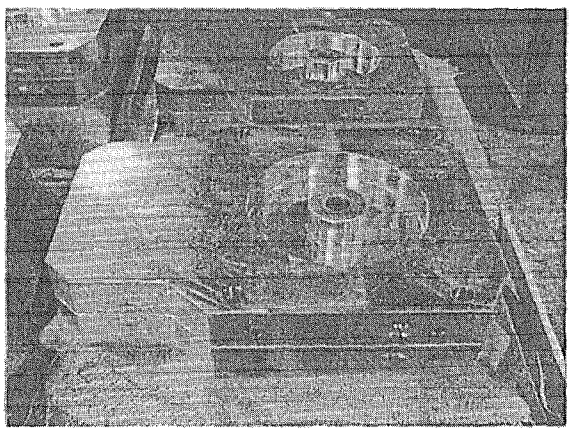

Figure 11. Finished brazed units.

The CCL completed a preliminary design review in November 2000. Many of the manufacturing steps have been verified, and initial definition and packaging has been done for the inter-segment diagnostics. A final design review is scheduled for next spring, and the procurement process for the copper assemblies will be initiated soon afterward.

5. RF-Power System

To reduce the cost of the RF system, we performed trade studies between number and power of klystrons, RF transmitters, power supplies, and cavity-control mechanisms. The final architecture, shown in the following table, is the result of these studies.

Table 7. Summary of linac RF architecture.

Structure	W_{final}	Total Length	Cells per Cavity	Cavities per Module	Modules	No of Klystrons	Structure Length
	MeV	m					m
DTL	86.8	36.6	60 to 21		6	6	36.6
CCL	185.6	91.9	8	12	4	4	55.4
SRF I	379.2	157.7	6	3	11	33	64.2
SRF II	948.7	276.0	6	4	15	59	118.4
SRF upgrade	1227.6	323.4	6	4	6	25	47.3

Structure	HVPS	HVPS Power	Transmitters	Klystrons	Klystron Power
		MW			MW
RFQ & DTL	3	10	7	7	2.5
CCL & HEBT	5	10	6	6	5.0
SRF I & II	8	10	16	92	0.55
SRF upgrade	3	10	5	25	0.60

Figure 12 shows schematically the layout of the linac RF system [18].

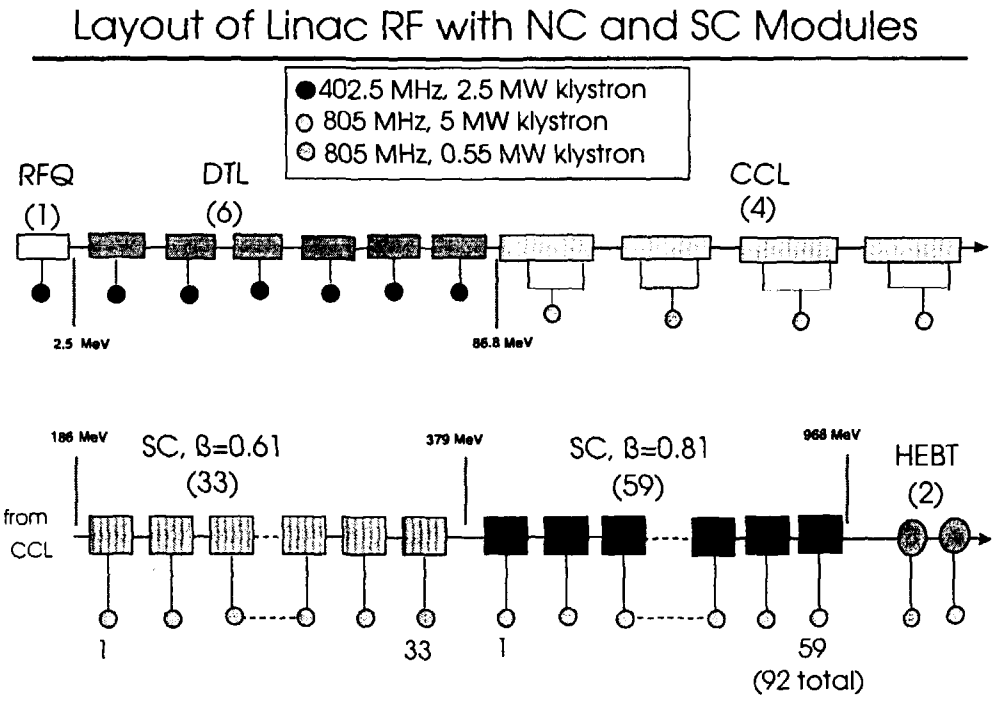

Figure 12. Layout of linac RF system with NC and SC modules

For the number and sizing of the SRF klystrons, we assumed the saturated power output should be 33% above the power needed by the cavity plus beam. Microphonics and Lorentz-forces lead to frequency variations of about 300 to 400 Hz, total. This varies the cavity amplitude response by up to 9% and phase by up to 12° at the maximum. The combination of amplitude and phase variation is a loss of output capability of as much as 12%. The remaining overhead is about 11%, which is needed for other errors and noise effects.

The RF control system [19] must maintain RF Fields to ±0.5% and ±0.5°. With one klystron per cavity, we can provide one control loop around each klystron/cavity pair. This provides the capability to compensate for the Lorentz forces and microphonics. We can, however, use one HV system and RF transmitter to serve several klystrons, as indicated in figure 13. A block diagram of the RF control system is shown in figure 14.

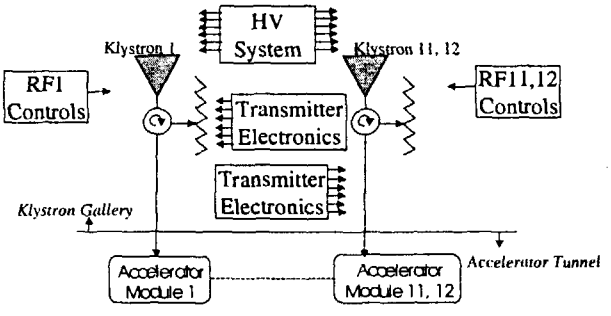

Figure 13. SCRF-system block diagram for 0.55-MW klystrons.

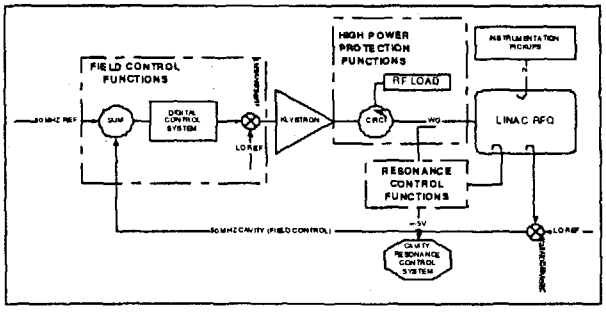

Figure 14. Simplified block diagram of the RF-control system.

Because we are powering klystrons with outputs from 0.55 to 5.0 MW, two basic types of HV systems are needed: a high-voltage version (~140 kV) and a lower-voltage version (~80 kV). Both have a nominal 10-MW peak power. The LANL-designed converter-modulator is the primary solution [20]. The design accommodates two or three 2.5-MW, 402.5-MHs klystrons (RFQ and DTL), one5-MW, 805-MHz klystron (CCL), or 11-12 550-KW, 805-MHz klystrons (SRF). The following table gives the klystron power distribution.

Table 8. Arrangement of the klystrons and power supplies

Frequency (MHz)	Klystron Power (MW)	Number of Klystrons	High Voltage (kV)	Current (A)	Klystrons per HV System
402.5	2.5	7	130	35	2
805	5.0	6	140	88	1
805	0,55	92	69	12.7	11 OR 12

A prototype of the converter-modulator is being assembled at Los Alamos, and testing will begin next year. The prototype includes three IGBT switch plate assemblies and a boost transformer. The control subsystem includes control and protection, an adaptive feed-forward and feedback system, interlocks, and a programmable logic controller.

6. Linac Physics and Simulations

The design of the SRF linac has been a collaborative effort between Los Alamos, ORNL, and Jefferson Lab [10-12]. Based on $E_{max} \leq 27.5$ MV/m, we made trade studies to determine the most cost-effective combination of cavities, cryostats, and RF systems to achieve reliable performance. The result was two cavity types, one optimized for a beta of 0.61 and the other for a beta of 0.81. A transition energy of ~375 MeV maximized the final energy for a fixed-cost machine [11]. Figure 15 shows the nominal klystron and cavity power.

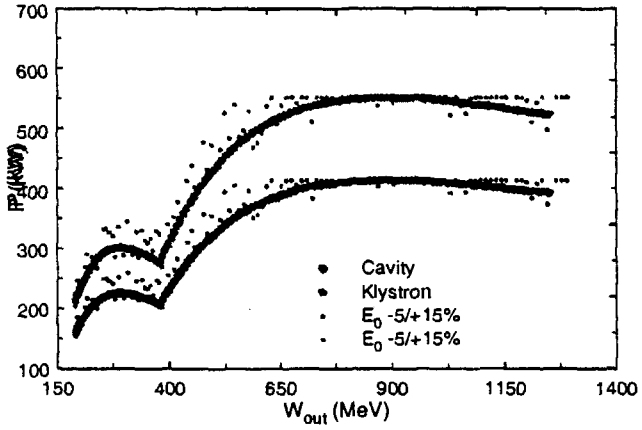

Figure 15. Graph of klystron (top) and cavity (bottom) power for the SCL. The solid lines are nominal values, and the dots are random distributions expected. For a large part of the SCL, the attainable energy gain is limited by the klystron power.

Following design of the basic SRF cavity structure, we optimized performance of the linac using the beam dynamics code PARMILA. An important part of these studies was determining the phase law for the SRF linac that maximized output energy while minimizing emittance growth. Before considering errors, we obtained solutions illustrated in figure 16.

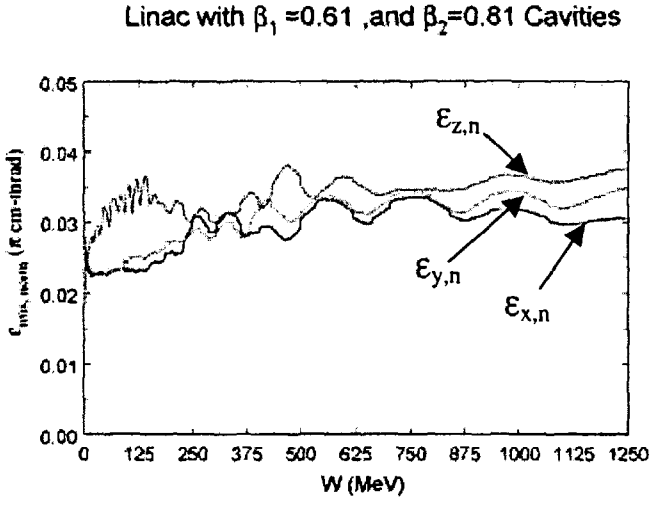

Figure 16. Normalized rms transverse and longitudinal emittance along the linac before considering any alignment errors.

Alignment errors cause the beam to be displaced from the linac axis and can magnify effects of nonlinear fields such as multipoles and gap fields. We studied the effect of errors individually to determine which of them contributed most to the displacement of the beam from the linac axis. The code LTRACE was used, which represents the beam by an ellipsoid and tracks the centroid of the beam. Figure 17 shows the probability distributions of the centroid excursion in the CCL for four individual error cases with random errors picked within the tolerance limits listed.

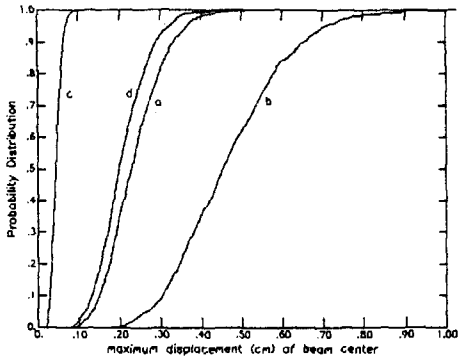

CCL tolerance limits:
a: Quad displacement = 0.005"
b: Quad displacement = 0.010"
c: Quad tilt = 5.0°
d: Tank displacement = 0.100"

Figure 17. Probability distribution of beam centroid excursion in the CCL for typical errors.

Clearly, for the CCL, the quad displacement is the most sensitive alignment error. We made similar studies for the SRF linac, as shown in Figure 18. For this case, the doublet tilt error is the most sensitive alignment error. We are continuing these studies and using them to set installation requirements for the linac.

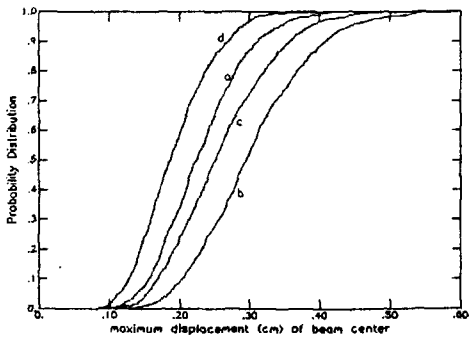

SRF linac tolerance limits:
a: Doublet displacement = 0.010 inch
b: Doublet tilt = 0. 01°
c: Quad tilt (wrt doublet axis) = 1.00°
d: Cavity displacement = 0.050 inch

Figure 18. Probability distribution of beam centroid excursion in the SRF linac for typical errors.

RMS emittance profiles, with and without errors, as functions of β are shown in the following figure. A growth in emittance is observed at the transition region between the CCL and SRF structures (at $\beta = 0.54$). This is due to the abrupt change in the lattice-period length accompanied by the design choice of requiring a smooth and continuous value for the transverse-focusing strength per unit length across the transition. The final emittance, however, is within the limit of 0.50 π-mm-mrad.

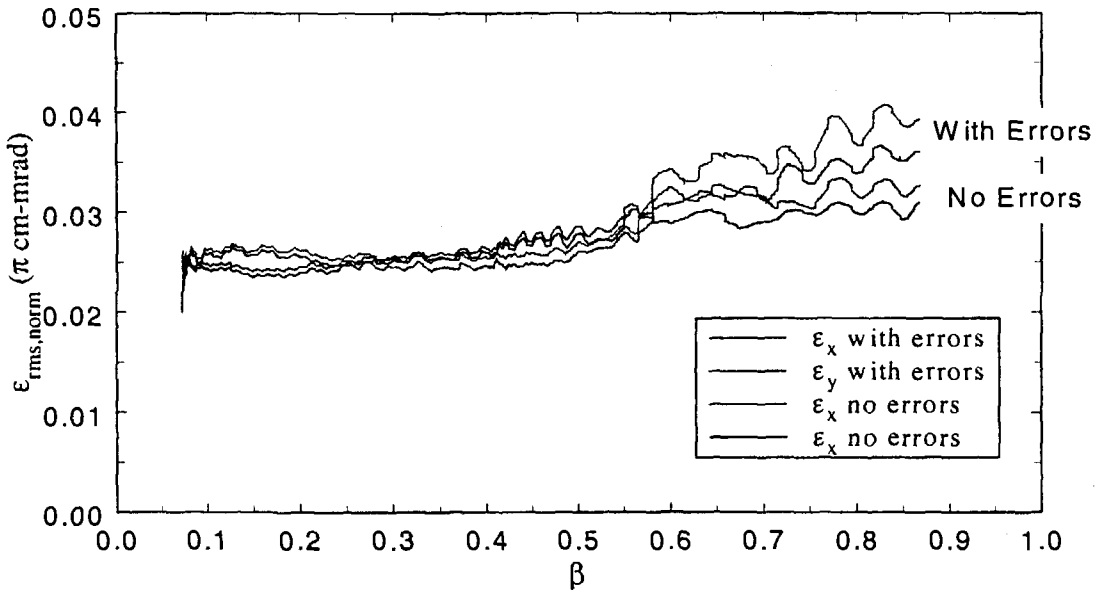

Figure 19. RMS transverse emittance as functions of β for simulations with and without errors in the linac. In each set of curves (with and without errors), the top curve is the x emittance and the bottom curve is the y emittance.

Figure 20 shows the real- and phase-space distributions at the end of the SRF linac using the 3-D space-charge code PICNIC [21].

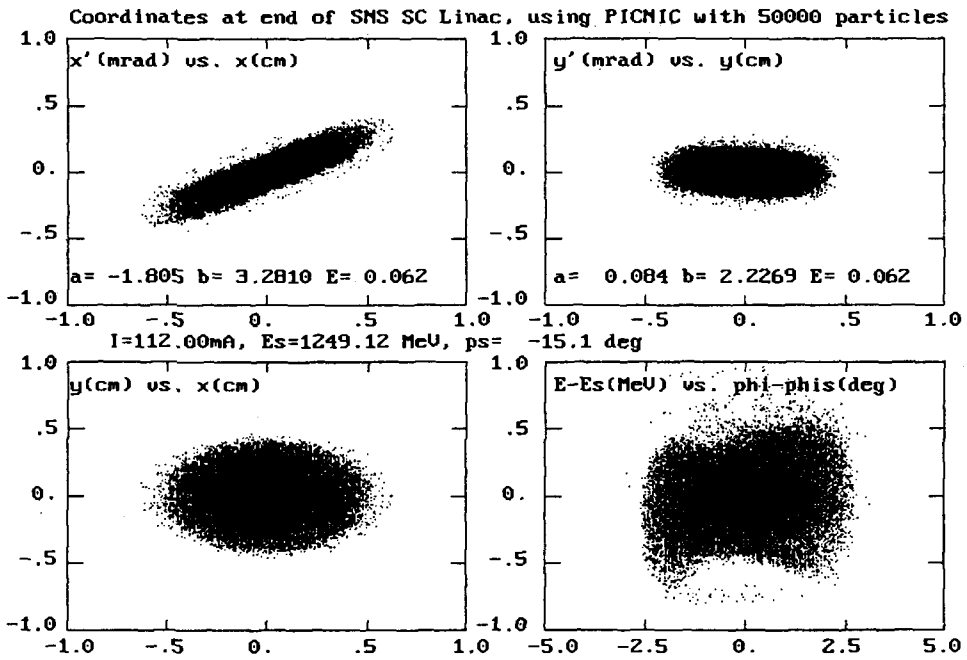

Figure 20. Real- and phase-space distributions at the end of the SRF linac using the 3D space-charge code PICNIC.

7. Diagnostics and Commissioning Planning

Diagnostics are an important part of a high-intensity linac. Accurate steering and matching of the beam are required to limit beam loss on apertures that would lead to activation and prevent hands-on maintenance [22, 23]. A description of the diagnostic suite for the SNS linac has been published [24]. The following is a list of the types of diagnostics under design.

- Beam position and phase monitor (BPM)
- Profile monitor (wire scanner and harp)
- Current monitor (toroid)
- Loss monitor (ionization chamber)
- Beam-in-gap detector (laser ionization)
- Phase width detector (Fourier)

The beam-in-gap detector uses a Q-switched laser to strip the H^- beam in the 90-degree bend between the linac and the accumulator ring. Stripped beam is detected at a downstream detector. The timing of the laser is synchronized with the chopping frequency so that one can detect the ratio of beam intensity in the pulse to that between pulses. The goal is to measure this ratio to an accuracy of 10^{-4}. A description of this system has been published [25].

Calculations supporting the design of the beam position and phase monitors have also been published [26,27]. The limited space in the low-energy regions of the linac has led to novel applications of BPM technology. We plan to insert BPMs in some of the empty drift tubes of the FF0DD0 lattice of the DTL, analyzing the second harmonic of the 402.5-MHz beam frequency (805-MHz). A prototype DTL BPM mechanical design is shown below.

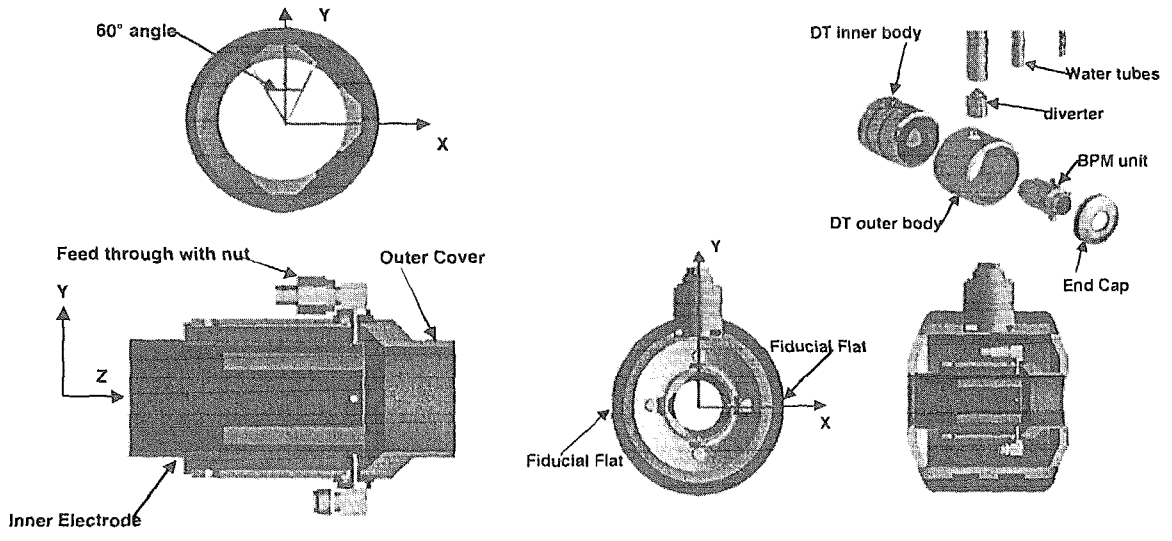

Figure 21. Assembly and exploded views of BPM to fit inside drift tubes of the DTL.

The physics design of a diagnostic-plate for commissioning of the linac has started, with a layout as shown in Figure 22. Commissioning scenarios have been developed for setting phase and amplitude of the RF cavities and for determining beam parameters. After the first

DTL tank we plan to run full duty-factor beam into a 16-kW portable beam dump, but for higher-energy modules the commissioning will be limited to low duty factors.

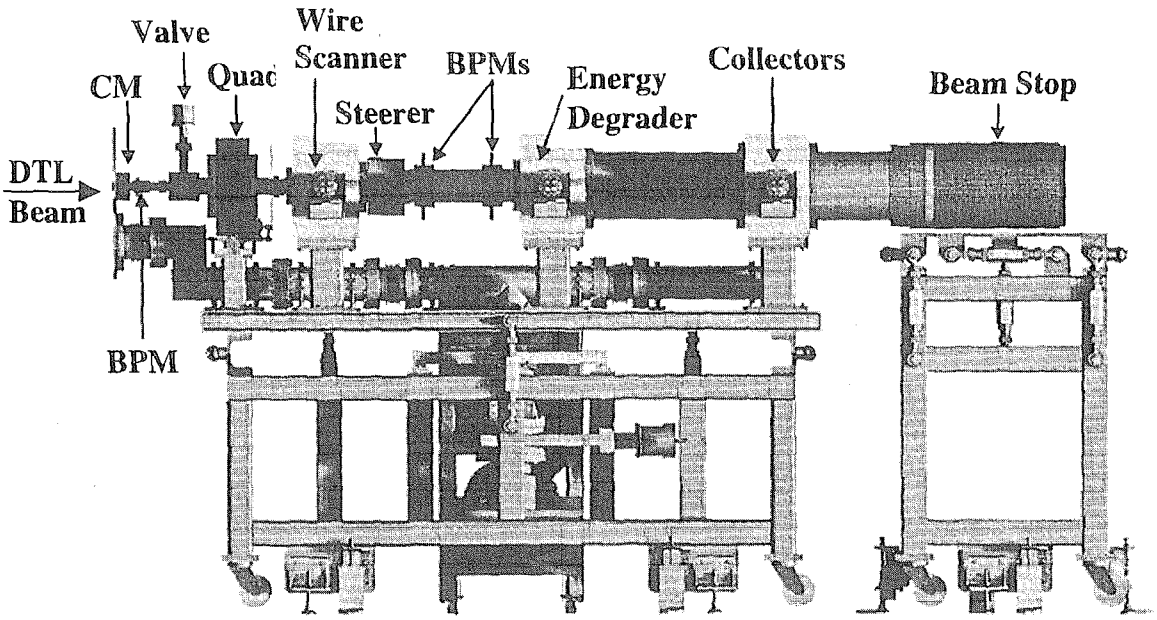

Figure 22. Preliminary layout of diagnostic plate for commissioning DTL Tank 1.

Acknowledgements

Many people contributed material for preparation of this paper. The author attempted to include most of these in the references, but some may have inadvertently been omitted, or their work has not yet been published. In addition to those cited, other references and contributors can be found in publications, technical notes, and progress reports for the SNS linac at http://www.mesa53.lanl.gov/sns/.

References

[1] B. Appleton, "The National Spallation Neutron Source," Proceedings Of the Particle Accelerator Conference (PAC'97), Vancouver, BC, May 1997. 20.

[2] J. Alonso, "Status Report on the Spallation Neutron Source (SNS) Project," Proceedings of the European Particle Accelerator Conference (EPAC98), Stockholm, Sweden, June 1998.

[3] A. Jason, "A Linac for the SNS," Proceedings of the 1998 Linac Conference, Chicago, IL, August 1998, 415.

[4] R. Hardekopf, "Linac Design for the SNS," Proceedings of the Second Intl. Topical Meeting on Nuclear Applications of Accelerator Technology, Gatlinburg, TN, September 1998, 208.

[5] R. Hardekopf, D. Stout, and T. Sutton, "Project Status of the 1-GeV SNS Linac," Proceedings of the 1999 Particle Accelerator Conference, New York, NY, March 1999, 3597.

[6] J. Billen, H Takeda, T. Bhatia, "Linac RF Structures for the SNS," PAC99, New York, NY, March 1999, 3585.

[7] N. Bultman, Z. Chen, M. Collier, J. Erickson, A. Guthrie, W. Hunter, T. Ilg, R. Meyer, N. Snodgrass, "Mechanical Engineering of the Linac for the SNS," PAC99, New York, NY, March 1999, 3594.

[8] M. Lynch, P. Tallerico, W. Reass, SNS RF System Overview," PAC99, New York, NY, March 1999, 453.

[9] R. L. Kustom, "An Overview of the Spallation Neutron Source Project," Proceedings of the XX International Linac Conference, Monterey, CA, August 2000 (to be published).

[10] J. Stovall, S. Nath, H. Takeda, J. Billen, L. Young, M. Lynch, D. Rees, J. Galambos, D. Jeon, D. Raparia, J. Wei, R. Sundelin, K. Crandall, C. Pagani, P. Pierini, "Superconducting Linac for the SNS," Proceedings of the XX International Linac Conference, Monterey, CA, August 2000 (to be published).

[11] J. Galambos, J. Stovall, S. Nath, H. Takeda, J. Billen, L. Young, J. Jeon, J. Wei, K. Crandall, "The SNS Superconducting Linac Architecture," Proceedings of ICANS-XV," Tsukuba, Japan, November 2000 (these proceedings).

[12] R. Sundelin, "Superconducting Linac," Proceedings of ICANS-XV," Tsukuba, Japan, November 2000 (these proceedings).

[13] R. Keller, "State of the SNS Front-End Systems," Proceedings of the XX International Linac Conference, Monterey, CA, August 2000 (to be published).

[14] J. Staples, D. Oshatz, T. Saleh, "Design of the SNS MEBT," Proceedings of the XX International Linac Conference, Monterey, CA, August 2000 (to be published).

[15] S Kurennoy, J. Power, and D. Schrage, "Meander-Line Current Structure for SNS Fast Beam Chopper," PAC99, New York, NY, March 1999, 1399.

[16] S. Kurennoy, J. Power, "Development of Meander-Line Current Structure for SNS Fast 2.5-MeV Beam Chopper," European Particle Accelerator Conference, Vienna, Austria, July 2000 (to be published).

[17] S. Kurennoy, J. Power, "Meander-Line Current Structure Development for SNS Fast Chopper," International Linac Conference, Monterey, CA, August 2000 (to be published).

[18] M. Lynch, W. Reass, D. Rees, A. Regan, P. Tallerico, "The Spallation Neutron Source (SNS) Linac RF System," International Linac Conference, Monterey, CA, August 2000 (to be published).

[19] A. Regan, S. Kwon, T. Rohley, Y. Wang, M. Prokop, D. Thomson, "Design of the SNS Normal Conducting Linac RF Control System," International Linac Conference, Monterey, CA, August 2000 (to be published).

[20] W. Reass, J. Doss, R. Gribble, M. Lynch, P. Tallerico, Progress on the 140 kV, 10-Megawatt Peak, 1-Megawatt Average, Polyphase Quasi-Resonant Bridge, Boost Converter/Modulator for the Spallation Neutron Source (SNS) Klystron Power System, International Linac Conference, Monterey, CA, August 2000 (to be published).

[21] N. Pichoff, S. Nath, and J. M. Lagniel, Proceedings of the 1998 Linac Conference, Chicago, IL, August 1998, 141.

[22] R. Hardekopf, "Beam Loss and Activation at LANSCE and SNS," ICFA Conference on High-Intensity, High-Brightness Beams, Lake Geneva, WI, September 1999 (to be published).

[23] J. Alonso, "Beam Loss Working Group Report," ICFA Conference on High-Intensity, High-Brightness Beams, Lake Geneva, WI, September 1999 (to be published).

[24] R. Hardekopf, "Beam Diagnostic Suite for the SNS Linac," LA-UR-00-2282, Beam Instrumentation Workshop, Boston, May 2000 (to be published).

[25] R. Shafer, "Laser Diagnostic for High-Current H^- Beams," Proceedings of the 1998 Linac Conference, Chicago, IL, August 1998, 535.

[26] S. Kurennoy, "Electromagnetic Modeling of Beam Position and Phase Monitors for SNS Linac," Beam Instrumentation Workshop, Boston, May 2000 (to be published).

[27] S. Kurennoy, "Beam Position-Phase Monitors for SNS Linac," Proceedings of the XX International Linac Conference, Monterey, CA, August 2000 (to be published).